Journal of Materials Chemistry A

COMMUNICATION

View Article Online
View Journal | View Issue



Cite this: J. Mater. Chem. A, 2019, 7, 12434

Received 17th March 2019
Accepted 28th April 2019

DOI: 10.1039/c9ta02886b

rsc.li/materials-a



# A highly efficient alkaline HER Co–Mo bimetallic carbide catalyst with an optimized Mo d-orbital electronic state†

Gejun Liu,‡[a] Haipeng Bai,‡[a] Yujin Ji,[b] Lie Wang,[a] Yunzhou Wen,[a] Haiping Lin,[b] Lirong Zheng,[c] Youyong Li,[b] Bo Zhang*[a] and Huisheng Peng*[a]

Efficient catalysts for the alkaline hydrogen evolution reaction are continuously pursued to accelerate the kinetics of water splitting and enhance the conversion of renewable energy to chemical feedstock. Among numerous candidates, noble-metal-free $Mo_2C$ catalysts are favored because of their low cost, abundance and similar d-orbital electronic state to the state of the art platinum. However, due to the high empty d-orbital density of high-valence Mo species in $Mo_2C$, the HER performance was impaired. We reason that introducing modulators into the $Mo_2C$ framework that could decrease the empty d-orbital density and valence states of Mo may be an efficient way to optimize the HER energetics. Herein, inspired by the versatile electronic structures of 3d metals, we carried out first principles calculations using 3d metal Co as a dopant of $Mo_2C$ to construct Co–Mo bimetallic carbide and found an enhanced HER activity after Co incorporation. We further synthesized a Co–Mo bimetallic carbide catalyst. The obtained catalysts achieved excellent alkaline HER performance with the lowest overpotential of −46 mV at −10 mA $cm^{-2}$, a low Tafel slope of 46 mV $dec^{-1}$ and great stability without any decay after a 500 hour reaction. The X-ray adsorption spectroscopy study showed that the valence state of Mo was decreased by the Co dopant and we propose that the decrease of Mo valence states should be the reason for the better HER performance of the bimetallic carbide than bulk $Mo_2C$.

To minimize energy consumption in electrochemical water splitting, great efforts have been made to enhance the catalytic activity of hydrogen evolution reaction (HER) catalysts.[1–3] Alkaline electrolysis is considered to be more promising, because many abundant oxygen evolution reaction (OER) catalysts at the counter electrodes exceed noble-metal based catalysts in alkaline electrolytes[4–7] and the corrosion of electrolysis equipment can be avoided.[8] However, due to the pretty low concentration of protons in alkaline medium,[9] the HER becomes more sluggish than under acidic and neutral conditions.[10–13] It is now well-known that the Pt/C catalyst was the most efficient HER catalyst in alkaline medium; however, the high cost of the noble metal hinders its usage. Owing to their similar d-band electronic structure to that of Pt/C, molybdenum carbides ($Mo_2C$) have been applied in the alkaline HER and identified as one of the promising low-cost and effective substituents for noble metal catalysts.[14,15] However, their catalytic performance was encumbered by the intrinsic drawbacks like high empty d-orbitals density, leading to high-valence Mo species that are inactive for the HER.[14,16–21] Introducing a third element into $Mo_2C$ as a substituent for C atoms or Mo atoms is a promising strategy to overcome the intrinsic high empty orbital density of $Mo_2C$. Recently, nitrogen (N),[22–24] phosphorus (P),[25] sulfur (S)[26] and co-doped[27,28] $Mo_2C$ that involved the substitution of C atoms were reported to show better HER performance than bulk $Mo_2C$. Meanwhile, rich-electron group VIII metals show good ability to modulate the valence electron density and improve the catalytic efficiency. For example, overlapped d-bands were found in the FeNi alloy and CoV catalyst for the HER and also found in optimizing the valence state of iron oxides for better Fenton reaction performance.[29–34] Among the group VIII elements, the cheap 3d metals including Fe, Co and Ni have the potential for large scale application.

Herein, with the advantages of a similar d-orbital electronic state of $Mo_2C$ to Pt and efficient electronic structure modification properties of group VIII 3d metals, we reason that incorporating Co into the $Mo_2C$ framework may be a good pathway to enhance HER activity. Before carrying out the experiment, first-principles calculations were implemented to investigate the effect of the Co dopant on $Mo_2C$. We constructed a simulated structure of Co–Mo bimetallic carbide with a Co/Mo ratio of

[a]State Key Laboratory of Molecular Engineering of Polymers, Department of Macromolecular Science, Laboratory of Advanced Materials, Fudan University, Shanghai, 200438, China. E-mail: penghs@fudan.edu.cn; bozhang@fudan.edu.cn
[b]Institute of Functional Nano & Soft Materials (FUNSOM), Jiangsu Key Laboratory for Carbon-Based Functional Materials & Devices, Soochow University, Suzhou, 215123, China
[c]Beijing Synchrotron Radiation Facility, Institute of High Energy Physics, Chinese Academy of Sciences, Beijing, 100049, China

† Electronic supplementary information (ESI) available. See DOI: 10.1039/c9ta02886b

‡ These authors contributed equally to this work.

1 : 1, *i.e.*, we substituted half of the Mo atoms in the $Mo_2C$ lattice with Co and the resultant catalyst was named CoMoC. The structure was further optimized *via* minimizing the formation energy. For comparison, bulk $Mo_2C$ was also constructed. We detected six low index surface models (namely, (100), (002), (101), (102), (110) and (103) surfaces) of $Mo_2C$ and CoMoC and compared their surface energies as given in Table S1.† It was found that the (002) surface of $Mo_2C$ has the lowest surface energy of 0.160 eV $Å^{-2}$ and the most stable surface of CoMoC is the (110) surface with a surface energy of 0.199 eV $Å^{-2}$. According to the Gibbs–Wulff principles, the (002) surface of $Mo_2C$ and the (110) surface of CoMoC nanoparticles are the most stable surface, thus being considered for the HER.[35,36] We compared the change of Gibbs free energy upon hydrogen adsorption $\Delta G_{H^*}$ on the $Mo_2C$–S (002) and CoMoC–S (110) surfaces at various hydrogen coverage. As shown in Fig. S1,† the $\Delta G_{H^*}$ was close to zero when the hydrogen coverage reached 50.0% on $Mo_2C$ and 16.7% on CoMoC, respectively.[37,38] The atomic structures of $Mo_2C$ and CoMoC at the above optimal H coverage, and their corresponding free-energy diagram are shown in Fig. 1a and c. The trend of HER activity with respect to the H coverage is dawn in Fig. 1b. As shown, at optimal H coverages, the $\Delta G_{H^*}$ on $Mo_2C$–S (002) and CoMoC–S (110) was −0.11 eV and −0.10 eV, respectively. This implies better HER performance on CoMoC (110) than that on $Mo_2C$ (002).

Based on the calculation results, we synthesized Co–Mo bimetallic carbide catalysts using a facile thermal treatment process (see the ESI† for details). Their elemental composition was quantified *via* inductively coupled plasma optical emission spectrometry (ICP-OES) analysis and energy dispersive spectroscopy (EDS) (Fig. S2, Table S2†), which demonstrated the ratio of Co, Mo and C to be ~1 : 1 : 1. The mass loading of the catalysts was quantified by both calculating the mass difference of Ni foam before and after the catalyst fabrication process and ICP-OES. The obtained mass loadings were 3.88 mg $cm^{-2}$ and 4.02 mg $cm^{-2}$, respectively. The optimized Co–Mo bimetallic carbide catalyst was also denoted as CoMoC, consistent with the constructed calculation model. To verify the effect of Co doping, the as-prepared $Mo_2C$ and Co (see the ESI† for details) were selected as contrast samples.

Unlike the platy structure of pristine $Mo_2C$,[16] the modified CoMoC was composed of uniform ~5 nm particles without obvious aggregation (Fig. 2a–c), which is in agreement with the morphology reported in previous work where introducing a second metallic element transformed bulk $Mo_2C$ into nanoparticles.[39] When compared with the platy-shaped and ~1 μm particle-shaped $Mo_2C$ and Co contrast catalysts (Fig. S3†), the nano-sized particle CoMoC catalyst can expose more active sites.[40] The high resolution TEM image (Fig. 2c) of partial enlarged Fig. 2b depicted clear lattice fringes with an interplanar distance of 0.21 nm, which is mostly in accordance with the interplanar distance of β-$Mo_2C$ (101) but a little smaller than that of β-$Mo_2C$ (0.23 nm). Moreover, the inserted selected area electron diffraction (SAED) further revealed the smaller interplanar distance of CoMoC than that of $Mo_2C$. The shrinkage of the catalyst interplanar distance revealed a smaller crystal cell of CoMoC than that of $Mo_2C$ as a result of the incorporation of Co atoms with a smaller atomic diameter than Mo atoms.[41,45,46]

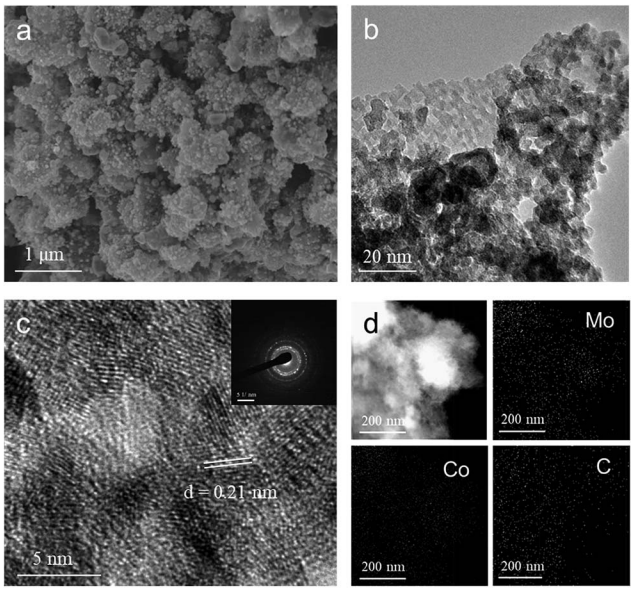


Fig. 2 Morphology characterization of the CoMoC catalyst after the HER. (a) SEM image of the as-prepared bimetallic carbide. (b) TEM image of the CoMoC catalyst. (c) High resolution TEM photo of the catalysts and inset SAED pattern. (d) TEM image and corresponding EDS elemental mappings for Mo, Co and C of the CoMoC catalyst.

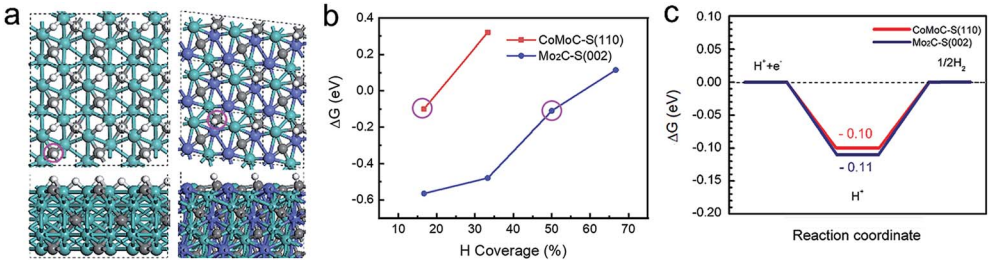


Fig. 1 DFT calculation results of the HER activity on $Mo_2C$ and CoMoC surfaces. (a) The configurations on $Mo_2C$–S (002) and CoMoC–S (110) at an H coverage of 50.0% and 16.7%, respectively. The typical adsorption site of H atoms is indicated with magenta circles. (b) The calculated Gibbs free energy of hydrogen adsorption ($\Delta G_{H^*}$) as a function of H coverage. The H coverages of configurations shown in (a) are highlighted with magenta circles. (c) Free-energy diagram of $\Delta G_{H^*}$ at the H coverages highlighted in (b). The gray, white, cyan and violet spheres represent C, H, Mo and Co atoms, respectively.

Meanwhile, homogeneous distribution of Mo, Co and C elements was further verified by EDS element mapping (Fig. 2d). Together, HRTEM, SAED and EDS mapping show evidence that the Co atoms were doped into $Mo_2C$ crystals and the formed Co–Mo bimetallic carbide has a smaller interplanar distance than $Mo_2C$.

Besides morphology characterization, the detailed structural information about CoMoC was also obtained. Different from the sharp and obvious main peak at $2\theta = 39^\circ$ of the $Mo_2C$ pattern (consistent with β-$Mo_2C$, PDF#35-0787) and Co foil pattern (PDF#15-0806) (Fig. S4†), the XRD patterns of the as-prepared CoMoC only show broadened peaks (Fig. 3a). The samples for XRD characterization were fabricated with an ultrasonic dispersion instrument to peel off the sample powder from the Ni foam (Fig. S5,† PDF#04-0850) for better comparison. The variation of XRD patterns indicated that the introduction of Co atoms into the unit cell led to the lattice distortion of the $Mo_2C$ crystal structure in the formation process of CoMoC. Meanwhile, the broadened peaks proved the nano-sized catalyst particles consistent with the morphology studies.[42,43] Furthermore, when the annealing time was extended from previous 3 hours to 4 hours, Co–Mo carbide with better crystallinity was obtained. The diffraction peaks of CoMoC (4 hours) shift to a higher angle and become much weaker than that of $Mo_2C$. The changes can be attributed to the doping of Co atoms in the $Mo_2C$ lattice, which can be concluded from many previous studies (Fig. S6†).[41,44–46] The structural difference between $Mo_2C$ and CoMoC was further investigated by using the Raman spectra. CoMoC showed an entirely different pattern compared with $Mo_2C$ (Fig. S7†).[47]

Further characterization was carried out to study the effects of Co atoms on the electronic structures of CoMoC. The Mo 4d X-ray photoelectron spectra (XPS) of CoMoC and $Mo_2C$ (Fig. 3b) suggest complicated 4d orbits with varied valence states of Mo on the surface of carbides, which is in accordance with the reported $Mo_2C$ XPS data.[48] The peak fitting results (Table S3†)

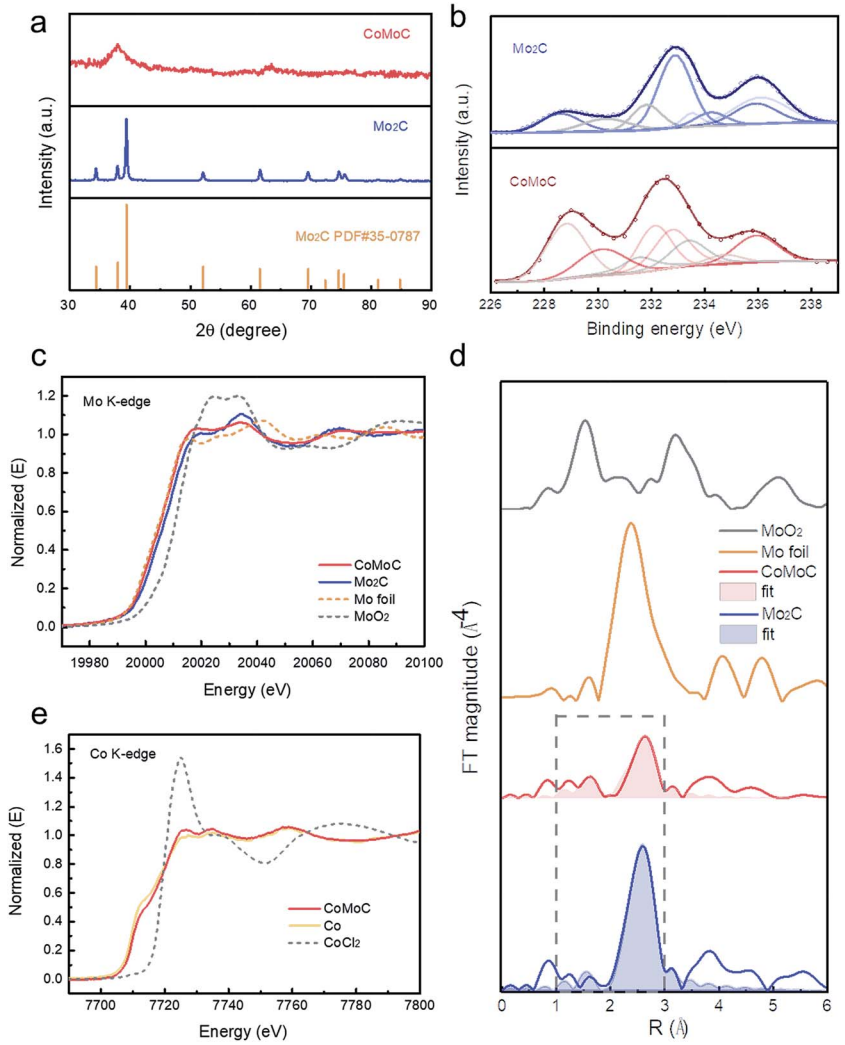


Fig. 3 Structural characterization of the CoMoC catalyst. (a) XRD patterns of CoMoC and contrast samples. (b) Mo 4d XPS data of CoMoC and β-$Mo_2C$. (c) XANES of the Mo K-edge of CoMoC, $Mo_2C$ and Mo foil. (d) $k^3$-weighted EXAFS Fourier transform magnitudes and first-shell fit of the Mo K-edge obtained from $Mo_2C$, CoMoC and Mo foil. (e) XANES of the Co K-edge of CoMoC, $CoCl_2$ and Co foil.

 

showed the increased proportion of Mo with lower valence states in CoMoC than that in $Mo_2C$, that is, the introduction of Co atoms resulted in the decrease of high valence state Mo species.[14,49,50] The Mo 4d XPS data proved that the introduction of Co into $Mo_2C$ can modify the d-orbits of $Mo_2C$, causing the decrease of the valence state of Mo. Furthermore, the decrease of the Mo valence states revealed richer electrons around Mo atoms.

X-ray absorption fine structure (XAFS) spectroscopy was also carried out. The white line shape and fingerprint character of the Mo K-edge X-ray absorption near-edge structure (XANES) around 20 keV can be employed to extract information regarding the occurrence of different phases and d-orbital electronic states.[51–53] The valence state of Mo in CoMoC and $Mo_2C$ is located between those of Mo NPs and $MoO_x$ (Fig. S8†), which is in accordance with previous work.[51] The nuance of the valence state between CoMoC and $Mo_2C$, *i.e.*, the relatively lower valence states of Mo atoms in CoMoC, could be ascribed to the effect of Co, suggesting that the doping of Co in the $Mo_2C$ structure can cause the decrease of Mo valence states (Fig. 3c), which is in accordance with the XPS results (Fig. 3c). The valence states of Mo were stable during the HER process and over a long-term HER process, which was proved by *in situ* quick X-ray absorption fine structure (QXAFS) and *ex situ* Mo K-edge XAFS spectra at different HER processing times (Fig. S9†). The details of the Mo binding environment were described through the $k^3$-weighted extended X-ray absorption fine structure (EXAFS) analysis (Fig. 3d) and the parameters of the local structure were calculated from curve-fitting analysis (Table S4†) in the window of $R = 1$ to 3 Å. The differences among four samples, *i.e.*, $MoO_2$, Mo NPs, CoMoC and $Mo_2C$, indicated that the surrounding atomic structures of Mo are significantly different. According to the fitting result, the Mo–Mo bond length was 2.95 Å in CoMoC, which is a little smaller than that of $Mo_2C$ (2.96 Å), and larger than that in Mo NPs apparently. Meanwhile, the sharp decrease in Mo–Mo coordination of CoMoC ($N = 5.2$) compared with $Mo_2C$ ($N = 12$) further demonstrated the substitution doping of Co atoms into the $Mo_2C$ structure.[54,55] To verify the interaction of Co and Mo, Co K-edge XANES of CoMoC and contrast samples was also performed (Fig. 3e). The electron transfer was also proved *via* the higher valence of Co in CoMoC compared to that of Co particles. Above all, we reason that the prepared CoMoC should be Co doped $Mo_2C$ with a Co/Mo ratio of 1 : 1 and relatively poor crystallinity.

To verify the expected better HER performance of the catalyst with an optimized Co/Mo ratio (Fig. S10 and S11†) than that of the contrast samples, the electrocatalytic HER activity of the samples was examined in 1.0 M KOH solution, using calibrated Ag/AgCl (see the ESI† for details). From the linear sweep voltammetry curve (LSV, Fig. 4a), it is impressive that CoMoC showed a remarkably low overpotential of −46 mV at a current density of −10 mA $cm^{-2}$, which is comparable to that of the state of the art catalyst, while the overpotential of perused $Mo_2C$ and metallic Co was −146 mV and −211 mV at −10 mA $cm^{-2}$, respectively. The LSV was further normalized *via* the electrochemically active surface area (ECSA) that was quantified by double-layer capacitance measurements (Fig. S12 and S13†). Gas chromatography measurements revealed a faradaic efficiency of ~100% for $H_2$ (Fig. S14†). CoMoC (4 hours) showed an overpotential of −98 mV at a current density of −10 mA $cm^{-2}$, which is worse than that of CoMoC (3 hours) (Fig. S15†). The better performance of CoMoC (3 hours) can be attributed to both the low

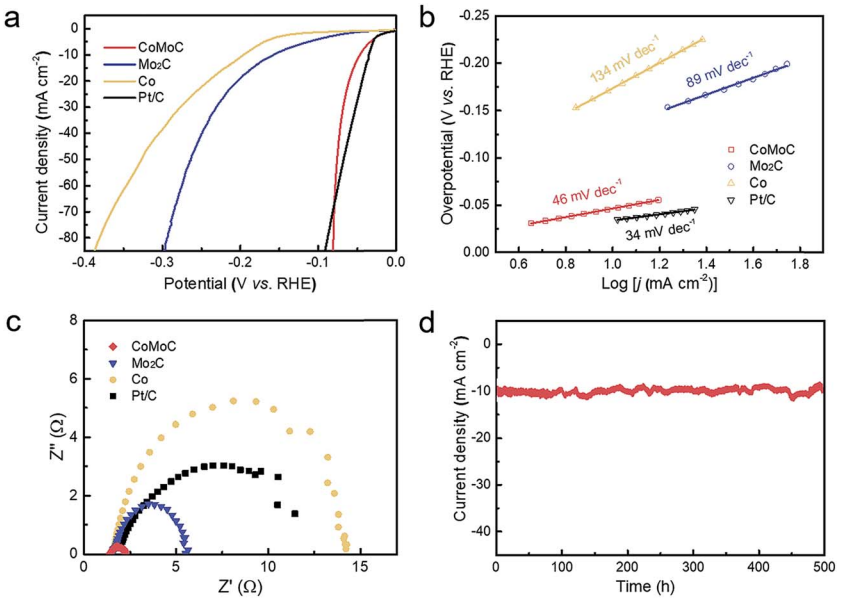


Fig. 4 HER performance of the CoMoC catalyst. (a) The LSV curves of CoMoC, $Mo_2C$, Co and Pt/C catalysts. (b) The Tafel plots of the CoMoC, $Mo_2C$, Co and Pt/C catalysts. (c) The Nyquist plots of CoMoC, $Mo_2C$, Co and Pt/C catalysts. (d) The stabile operation of the CoMoC catalyst running at −46 mV.

crystallinity and small grain size.[56,57] We also examined the acidic HER activity of CoMoC in 0.5 M $H_2SO_4$ and CoMoC showed a low overpotential of −100 mV, better than the performance of reference $Mo_2C$, exhibiting the intrinsic superiority of CoMoC in the HER (Fig. S16†).

Besides the overpotential, the Tafel slope is widely used to represent the kinetic performance of the HER. As shown in Fig. 4b, the CoMoC catalyst shows the smallest Tafel slope of 46 mV $dec^{-1}$, compared to 89 mV $dec^{-1}$, 134 mV $dec^{-1}$ and 34 mV $dec^{-1}$ of $Mo_2C$, Co and Pt/C catalysts, respectively. Furthermore, an electrochemical impedance spectroscopy study was also conducted (Fig. 4c). The results showed that, at the same applied potential, the smaller charge transfer resistance leads to higher catalytic activity of CoMoC. To investigate the stability, we carried out both cyclic voltammetric (CV) and potentiostatic tests. From the LSV curves of the freshly prepared CoMoC catalyst and the catalyst after 10 000 CV cycles (Fig. S17†), the CoMoC catalyst showed great stability without any decay at −10 mA $cm^{-2}$ and only a 9 mV drop at −30 mA $cm^{-2}$ after 10 000 CV cycles. Meanwhile, we observed no appreciable increase in the current during 500 h operation at an overpotential of −46 mV (Fig. 4d). The stability test proved the great durability of the Co modulated $Mo_2C$ bimetallic carbide structure and HER performance. The dissolution of CoMoC during the stability test was fairly little, which was quantified *via* ICP-OES (Table S5†). And further morphology characterization proved the structural stability of CoMoC (Fig. S18†).

In conclusion, aiming to modulate the d-orbital electronic properties of $Mo_2C$ for better HER activity, we supposed that Co, as group VIII 3d metal, can be a great doping candidate. The DFT calculation indicated that CoMoC has better HER performance as a result of lower H coverage and smaller $\Delta G_{H^*}$ of balanced H adsorption. Based on the calculation results, we fabricated a Co–Mo bimetallic carbide catalyst, and obtained a remarkably low overpotential of −46 mV at −10 mA $cm^{-2}$, a Tafel slope of 46 mV $dec^{-1}$ and great stability up to 500 h in alkaline solution. Further studies revealed that the better performance was attributed to the introduced Co atoms inside the $Mo_2C$ crystal cells, which can bring about a decreased content of high valence Mo species with less HER activity than low valence Mo species.

## Conflicts of interest

There are no conflicts to declare.

## Acknowledgements

This work was supported by MOST (2016YFA0203302), NSFC (21875042, 21634003, 51573027, 51673043, 21604012, and 21805044), STCSM (18QA1400800, 16JC1400702, 17QA1400400, and 18QA1400700), SHMEC (2017-01-07-00-07-E00062) and the Yanchang Petroleum Group. This work has also benefited from the 1W1B beamline at the Beijing Synchrotron Radiation Facility. The TEM study in this work is supported by the Shanghai Institute of Ceramics of Chinese Academy of Science.

## References

1 G. Wu, K. L. More, C. M. Johnston and P. Zelenay, *Science*, 2011, **332**, 443–447.
2 J. Zhang, Z. Zhao, Z. Xia and L. Dai, *Nat. Nanotechnol.*, 2015, **10**, 444–452.
3 G. Liu, H. Bai, B. Zhang and H. Peng, *Chem.–Eur. J.*, 2018, **24**, 18271–18292.
4 B. Zhang, X. Zheng, O. Voznyy, R. Comin, M. Bajdich, M. García-Melchor, L. Han, J. Xu, M. Liu and L. Zheng, *Science*, 2016, **352**, 333–337.
5 G.-R. Zhang and S. Wöllner, *Appl. Catal., B*, 2018, **222**, 26–34.
6 U. De Silva, J. Masud, N. Zhang, Y. Hong, W. P. Liyanage, M. A. Zaeem and M. Nath, *J. Mater. Chem. A*, 2018, **6**, 7608–7622.
7 Y. Wu, Y. Meng, J. Hou, S. Cao, Z. Gao, Z. Wu and L. Sun, *Adv. Funct. Mater.*, 2018, **28**, 1801397.
8 T. Kou, T. Smart, B. Yao, I. Chen, D. Thota, Y. Ping and Y. Li, *Adv. Energy Mater.*, 2018, **8**, 1703538.
9 Y. Zheng, Y. Jiao, A. Vasileff and S. Z. Qiao, *Angew. Chem., Int. Ed.*, 2018, **57**, 7568–7579.
10 Y. Wang, H. Zhuo, X. Zhang, X. Dai, K. Yu, C. Luan, L. Yu, Y. Xiao, J. Li, M. Wang and F. Gao, *Nano Energy*, 2018, **48**, 590–599.
11 F. Li, G. F. Han, H. J. Noh, Y. Lu, J. Xu, Y. Bu, Z. Fu and J. B. Baek, *Angew. Chem., Int. Ed.*, 2018, **57**, 14139–14143.
12 M. Gong, D.-Y. Wang, C.-C. Chen, B.-J. Hwang and H. Dai, *Nano Res.*, 2015, **9**, 28–46.
13 F. Safizadeh, E. Ghali and G. Houlachi, *Int. J. Hydrogen Energy*, 2015, **40**, 256–274.
14 C. Lu, D. Tranca, J. Zhang, F. N. Rodri Guez Hernandez, Y. Su, X. Zhuang, F. Zhang, G. Seifert and X. Feng, *ACS Nano*, 2017, **11**, 3933–3942.
15 Y. Liu, G. Yu, G. D. Li, Y. Sun, T. Asefa, W. Chen and X. Zou, *Angew. Chem., Int. Ed.*, 2015, **54**, 10752–10757.
16 H. Ang, H. Wang, B. Li, Y. Zong, X. Wang and Q. Yan, *Small*, 2016, **12**, 2859–2865.
17 H. Lin, N. Liu, Z. Shi, Y. Guo, Y. Tang and Q. Gao, *Adv. Funct. Mater.*, 2016, **26**, 5590–5598.
18 L. Liao, S. Wang, J. Xiao, X. Bian, Y. Zhang, M. D. Scanlon, X. Hu, Y. Tang, B. Liu and H. H. Girault, *Energy Environ. Sci.*, 2014, **7**, 387–392.
19 J.-Q. Chi, W.-K. Gao, J.-H. Lin, B. Dong, J.-F. Qin, Z.-Z. Liu, B. Liu, Y.-M. Chai and C.-G. Liu, *J. Catal.*, 2018, **360**, 9–19.
20 Y. Zhang, Y. Wang, S. Jia, H. Xu, J. Zang, J. Lu and X. Xu, *Electrochim. Acta*, 2016, **222**, 747–754.
21 X. Wang, R. Su, H. Aslan, J. Kibsgaard, S. Wendt, L. Meng, M. Dong, Y. Huang and F. Besenbacher, *Nano Energy*, 2015, **12**, 9–18.
22 S. C. Abbas, Z. Peng, J. Wu, G. Anandhababu, D. D. Babu, Y. Huang, M. A. Ghausi, M. Wu and Y. Wang, *ChemElectroChem*, 2018, **5**, 1186–1190.
23 J.-Q. Chi, K.-L. Yan, W.-K. Gao, B. Dong, X. Shang, Y.-R. Liu, X. Li, Y.-M. Chai and C.-G. Liu, *J. Alloys Compd.*, 2017, **714**, 26–34.
24 X. Chen, J. Qi, P. Wang, C. Li, X. Chen and C. Liang, *Electrochim. Acta*, 2018, **273**, 239–247.

 

25 L. N. Zhang, S. H. Li, H. Q. Tan, S. U. Khan, Y. Y. Ma, H. Y. Zang, Y. H. Wang and Y. G. Li, *ACS Appl. Mater. Interfaces*, 2017, **9**, 16270–16279.
26 Z. Zhao, F. Qin, S. Kasiraju, L. Xie, M. K. Alam, S. Chen, D. Wang, Z. Ren, Z. Wang and L. C. Grabow, *ACS Catal.*, 2017, **7**, 7312–7318.
27 J. Luo, J. H. Im, M. T. Mayer, M. Schreier, M. K. Nazeeruddin, N. G. Park, S. D. Tilley, H. J. Fan and M. Gratzel, *Science*, 2014, **345**, 1593–1596.
28 D. Wang, T. Liu, J. Wang and Z. Wu, *Carbon*, 2018, **139**, 845–852.
29 Z. Y. Yu, Y. Duan, M. R. Gao, C. C. Lang, Y. R. Zheng and S. H. Yu, *Chem. Sci.*, 2017, **8**, 968–973.
30 T. G. Kelly, S. T. Hunt, D. V. Esposito and J. G. Chen, *Int. J. Hydrogen Energy*, 2013, **38**, 5638–5644.
31 T. Wang, X. Guo, J. Zhang, W. Xiao, P. Xi, S. Peng and D. Gao, *J. Mater. Chem. A*, 2019, **7**, 4971–4976.
32 S. R. Pouran, A. A. A. Raman and W. M. A. W. Daud, *J. Cleaner Prod.*, 2014, **64**, 24–35.
33 Z. Chen, Y. Song, J. Cai, X. Zheng, D. Han, Y. Wu, Y. Zang, S. Niu, Y. Liu and J. Zhu, *Angew. Chem., Int. Ed.*, 2018, **57**, 5076–5080.
34 K. Berndt, U. Marx and O. Brümmer, *Phys. Status Solidi B*, 1978, **90**, 487–496.
35 Y. Shang and L. Guo, *Adv. Sci.*, 2015, **2**, 1500140.
36 Y.-J. Wang, W. Long, L. Wang, R. Yuan, A. Ignaszak, B. Fang and D. P. Wilkinson, *Energy Environ. Sci.*, 2018, **11**, 258–275.
37 S. S. Chou, N. Sai, P. Lu, E. N. Coker, S. Liu, K. Artyushkova, T. S. Luk, B. Kaehr and C. J. Brinker, *Nat. Commun.*, 2015, **6**, 8311.
38 Y. Luo, L. Tang, U. Khan, Q. Yu, H. M. Cheng, X. Zou and B. Liu, *Nat. Commun.*, 2019, **10**, 269.
39 M. Nagai, A. M. Zahidul and K. Matsuda, *Appl. Catal., A*, 2006, **313**, 137–145.
40 D. Kong, H. Wang, J. J. Cha, M. Pasta, K. J. Koski, J. Yao and Y. Cui, *Nano Lett.*, 2013, **13**, 1341–1347.
41 K. Xiong, L. Li, L. Zhang, W. Ding, L. Peng, Y. Wang, S. Chen, S. Tan and Z. Wei, *J. Mater. Chem. A*, 2015, **3**, 1863–1867.
42 C. Liang, P. Ying and C. Li, *Chem. Mater.*, 2002, **14**, 3148–3151.
43 L. F. Pan, Y. H. Li, S. Yang, P. F. Liu, M. Q. Yu and H. G. Yang, *Chem. Commun.*, 2014, **50**, 13135–13137.
44 P. Xiao, X. Ge, H. Wang, Z. Liu, A. Fisher and X. Wang, *Adv. Funct. Mater.*, 2015, **25**, 1520–1526.
45 H. A. Al-Megren, S. L. González-Cortés, T. Xiao and M. L. Green, *Appl. Catal., A*, 2007, **329**, 36–45.
46 J. Cheng and W. Huang, *Fuel Process. Technol.*, 2010, **91**, 185–193.
47 T.-C. Xiao, A. P. E. York, H. Al-Megren, C. V. Williams, H.-T. Wang and M. L. H. Green, *J. Catal.*, 2001, **202**, 100–109.
48 C. Wan, Y. N. Regmi and B. M. Leonard, *Angew. Chem., Int. Ed.*, 2014, **53**, 6407–6410.
49 Y. Zhao, K. Kamiya, K. Hashimoto and S. Nakanishi, *J. Am. Chem. Soc.*, 2014, **137**, 110–113.
50 R. Ma, Y. Zhou, Y. Chen, P. Li, Q. Liu and J. Wang, *Angew. Chem., Int. Ed.*, 2015, **127**, 14936–14940.
51 W.-F. Chen, C.-H. Wang, K. Sasaki, N. Marinkovic, W. Xu, J. Muckerman, Y. Zhu and R. Adzic, *Energy Environ. Sci.*, 2013, **6**, 943–951.
52 G. Wang, J. A. Schaidle, M. B. Katz, Y. Li, X. Pan and L. T. Thompson, *J. Catal.*, 2013, **304**, 92–99.
53 T. Ressler, R. E. Jentoft, J. Wienold, M. M. Günter and O. Timpe, *J. Phys. Chem. B*, 2000, **104**, 6360–6370.
54 Q. Xiong, Y. Wang, P. F. Liu, L. R. Zheng, G. Wang, H. G. Yang, P. K. Wong, H. Zhang and H. Zhao, *Adv. Mater.*, 2018, 1801450.
55 J. Deng, H. Li, S. Wang, D. Ding, M. Chen, C. Liu, Z. Tian, K. Novoselov, C. Ma and D. Deng, *Nat. Commun.*, 2017, **8**, 14430.
56 B. Zhang, X. Zheng, O. Voznyy, R. Comin, M. Bajdich, M. García-Melchor, L. Han, J. Xu, M. Liu and L. Zheng, *Science*, 2016, **352**, 333–337.
57 M. Qamar, A. Adam, B. Merzougui, A. Helal, O. Abdulhamid and M. Siddiqui, *J. Mater. Chem. A*, 2016, **4**, 16225–16232.